

Phonon-Glass and Heterogeneous Electrical Transport in A-site Deficient SrTiO₃

S. R. Popuri,¹ R. Decourt,^{2,3} J.A. McNulty,⁴ M. Pollet,^{2,3,§} A. D. Fortes,⁵ F.D. Morrison,^{4,&} M.S. Senn,^{6,‡} and J.W.G. Bos^{1,*}

¹*Institute of Chemical Sciences and Centre for Advanced Energy Storage and Recovery, School of Engineering and Physical Sciences, Heriot-Watt University, Edinburgh, EH14 4AS, UK.*

²*CNRS, ICMCB, 87 avenue du Dr. A. Schweitzer, Pessac F-33608, France*

³*Université de Bordeaux, 87 avenue du Dr. A. Schweitzer, Pessac F-33608, France*

⁴*EaStCHEM School of Chemistry, University of St Andrews, St Andrews, KY16 9ST, UK*

⁵*ISIS Facility, Rutherford Appleton Laboratory, Harwell Campus, Didcot, OX11 0QX, UK*

⁶*Department of Chemistry, University of Warwick, Gibbet Hill, Coventry, CV4 7AL, UK*

Corresponding author: *: j.w.g.bos@hw.ac.uk

§: michael.pollet@icmcb.cnrs.fr; &: finlay.morrison@st-andrews.ac.uk; ‡: m.senn@warwick.ac.uk;

Abstract

The phonon-glass electron crystal concept is one of the key guiding principles for the development of efficient thermoelectric materials. Here, we confirm that SrTiO₃ becomes a phonon-glass for large numbers of A-site vacancies in the Sr_{1-x}La_{0.67x}□_{0.33x}TiO₃ series and show that its electron crystal properties are stymied by the presence of a core-shell grain structure. Thermal conductivity, heat capacity and neutron powder diffraction, complemented by representational analysis and phonon calculations, were used to investigate the thermal transport. This reveals that the heat carrying modes are dominated by Sr motions and that these become more localised upon the introduction of the A-site vacancies, consistent with the observed phonon-glass state. Impedance spectroscopy and DC electrical measurements were used to probe the electrical properties of insulating and conducting samples. This reveals the coring of grains due to oxidation on cooling from sintering temperatures. The resultant insulating shell limits the thermoelectric power factor to $S^2/\rho = 0.45 \text{ mW m}^{-1} \text{ K}^{-2}$ and the figure of merit to $ZT = 0.15$ at 900 K for Sr_{0.20}La_{0.53}□_{0.27}Ti_{0.95}Nb_{0.05}O_{3-δ}. The thermal properties of these materials are therefore controlled by

an intrinsic feature of the microstructure (i.e. the A-site vacancies), while the electrical properties are grain boundary limited, which in principle can be controlled independently to raise S^2/ρ and ZT .

Introduction

The design of phonon glass electron crystal (PGEC) materials has been one of the key guiding concepts of modern thermoelectrics research.¹ The aim is to create materials with the good electrical properties of crystalline solids but with the low thermal conductivity of a structural glass. If this can be achieved, then high thermoelectric figures of merit, $ZT = (S^2/\rho\kappa)T$ and efficient waste heat recovery become possible.²⁻³ Here, S is the Seebeck coefficient, ρ is the electrical resistivity and the thermal conductivity κ is the sum of lattice and electronic components. Classical examples of PGEC materials are host-guest materials,⁴⁻⁷ such as clathrates and skutterudites that consist of a framework for electrical conduction and loosely bound rattling atoms that reduce the thermal conductivity.⁸⁻¹⁰

SrTiO_3 is one of the best explored oxide thermoelectric materials with peak $ZT = 0.4$ at high temperatures.¹¹⁻¹⁸ It is characterised by large power factors $S^2/\rho \leq 3 \text{ mW m}^{-1} \text{ K}^{-2}$ at $\sim 500 \text{ K}$ in single crystals.¹⁹⁻²⁰ The limitation is the relatively large $\kappa_{\text{lat}} \sim 10 \text{ W m}^{-1} \text{ K}^{-1}$ near room temperature,²¹⁻²² which is far larger than the $\kappa_{\text{lat}} \sim 1 \text{ W m}^{-1} \text{ K}^{-1}$ that is desirable to achieve high ZT values. For this reason, great effort has been expended to reduce κ_{lat} via substitutions on the Sr and Ti sites and through oxygen deficiency.²³⁻²⁵ This work has led to a substantial reduction to $\kappa_{\text{lat, RT}} \sim 3-4 \text{ W m}^{-1} \text{ K}^{-1}$ but always maintained a T^{-z} temperature dependence,²⁶ typical of crystalline materials.

Recently, we used A-site vacancies in the $\text{Sr}_{1-x}\text{La}_{0.67x}\square_{0.33x}\text{TiO}_3$ perovskites to manipulate the thermal transport, leading to the emergence of a phonon-glass state for samples with 27% vacancies ($x = 0.8$),²² since confirmed by others.^{13, 27-29} In principle, this sublattice engineering allows for the decoupling of the electrical and thermal transport as it leaves the conducting Ti-O framework unaffected. However, we found that samples with large amounts of A-site vacancies had reduced S^2/ρ due to the emergence of a semiconducting tail near room temperature, thus limiting the overall

gain in performance.^{22, 30} Here, we provide further insight into the origin of both the phonon-glass and “reduced” electron crystal properties of A-site deficient SrTiO₃. The introduction of A-site vacancies leads to a large mass disorder parameter $\Gamma = 0.49$ for 27% vacancies, which is far larger than attained by conventional alloying (e.g. mixing Sr and La with $\Gamma_{\max} = 0.08$), suggesting that structural disorder is an important factor. However, at the same time, a large fraction of the Sr-O chemical bonds is broken, and this is expected to lead to a localisation of the phonon modes involving Sr. Recently, a near identical transition to phonon-glass behaviour was observed in Na_{0.5}La_{0.5}TiO₃,³¹ where Sr has been replaced by an equal mixture of Na⁺ and La³⁺. This leads to a similar mass disorder parameter ($\Gamma = 0.54$) but phonon calculations also point towards a localisation of the lattice vibrations due to the highly divergent (weak/strong) Na-O and La-O bond strengths. In terms of the electron crystal properties: our results on conducting Sr_{1-x}La_{0.67x}□_{0.33x}Ti_{1-y}Nb_yO_{3-δ} samples reveal an increase to $S^2/\rho \sim 1.3 \text{ mW m}^{-1} \text{ K}^{-2}$ at 500 K for 7% vacancies ($y = 0.05$) followed by a gradual decrease to $\sim 0.15 \text{ mW m}^{-1} \text{ K}^{-2}$ at 800 K for 27% vacancies ($y = 0.2$).²² By contrast, the Na_{0.5}La_{0.5}TiO₃ phonon-glass system does not show this strong reduction in S^2/ρ , demonstrating that it is possible to maintain the good electrical properties of SrTiO₃.³¹ Here, we demonstrate that the loss of electron crystal behaviour in A-site deficient samples is caused by the presence of a heterogeneous core-shell grain microstructure, which increases the electrical resistivity.

Methods

Polycrystalline Sr_{1-x}La_{0.67x}□_{0.33x}TiO₃ ($x = 0, 0.4$ and 0.8) samples were prepared on a 3-gram scale by heating cold pressed pellets containing ground mixtures of SrCO₃ (Alfa Aesar, 99.99%), La₂O₃ (Sigma-Aldrich 99.99%) and TiO₂ (Alfa Aesar, 99.99%) at 1200 °C for two times 12 hours, and at 1400 °C for 4 hours in air, with intermediate regrinding between steps. 1% excess SrCO₃ was used for the $x = 0.4$ and $x = 0.8$ samples to suppress the formation of a TiO₂ impurity phase. Oxygen deficient and Nb substituted Sr_{0.20}La_{0.53}□_{0.27}Ti_{1-y}Nb_yO_{3-δ} ($0 \leq y \leq 0.15$; Nb₂O₅ from Alfa Aesar, 99.9985%) samples were prepared in a similar manner, but all heating steps were done under 5% H₂

in N₂ with the samples placed on graphite disks. The final heating step for these samples was 1450 °C for 4 hrs. The densities of the sintered pellets are 92-95% of the theoretical values (see Table S1).

Laboratory X-ray powder diffraction data were collected on a Bruker D8 Advance diffractometer with Cu K_{α1} radiation. X-ray diffraction patterns (8 hr data collection) for all samples are shown in Figure S1 in the Supplementary Information. The microstructure and homogeneity of a Sr_{0.2}La_{0.53}□_{0.27}TiO₃ sample sintered in air was examined using a Quanta 650 FEG Scanning Electron Microscope. This showed the sample to be well sintered with large grains and a uniform elemental distribution (Figure S2).

Temperature dependent neutron powder diffraction (NPD) data were collected on an 8-gram Sr_{0.2}La_{0.53}□_{0.27}TiO₃ sample (sintered in air) using the time-of-flight High Resolution Powder Diffractometer (HRPD), equipped with a closed-cycle refrigerator (4-290 K) and furnace (300-1000 K), at the ISIS neutron and muon source, UK. Rietveld fits were performed using the GSAS/EXPGUI programmes.³²

Low-temperature thermal conductivity measurements were made using the Thermal Transport Option of a Quantum Design Physical Property Measurement System (PPMS). The heat capacities of SrTiO₃ and Sr_{0.2}La_{0.53}□_{0.27}TiO₃ (both sintered in air) were measured between 2 and 300 K using the heat capacity option of the PPMS. High temperature thermal diffusivity (α) and heat capacity (C_p) were measured using a Netzch LFA 457 and Perkin Elmer DSC 8500. The thermal conductivity was evaluated from the heat capacity and diffusivity data using: $\kappa = \alpha(T)C_p(T)d$, where d is the sample density. The measured κ were corrected for porosity (ϕ) using $\kappa/\kappa_{\text{dense}} = 1 - (4/3)\phi$, where ϕ was obtained from the gravimetric density. Electrical resistivity and Seebeck measurements were made using a Linseis LSR-3 instrument under a He atmosphere. Impedance spectroscopy was carried out on ceramic pellets over the frequency range 5 Hz - 13 MHz using an HP4192A Impedance Analyser under an applied ac voltage of 100 mV. Ag paint electrodes (RS components) were applied to opposing pellet faces and cured at 120 °C for 20 minutes. Samples were mounted in

a sample holder of in-house design and placed in a non-inductively wound tube furnace allowing data to be collected from ambient to 923 K. All data were subsequently corrected for sample geometry (electrode area and sample thickness); as a result, resistance (R) values extracted by modelling on equivalent circuits consisting of RC elements (discussed below) correspond to resistivities.

Symmetry analysis of the atomic displacement at the high-symmetry points in the Brillouin zone were done using the web based program ISODISTORT using the $Pm-3m$ perovskite, with a setting placing the A-site at the origin of the unit cell as the parent reference structure.³³

Phonon Eigen vector and values of high symmetry SrTiO_3 were calculated using CASTEP³⁴ in the density functional perturbation theory (DFPT) approximation³⁵ for 28 points in reciprocal space.

For the DFT calculations we used the GGA PBEsol exchange correlation functional³⁶ with norm-conserving pseudo potentials with a plane wave basis set cut-off energy of 600 eV and an $8 \times 8 \times 8$ k-grid with respect to the cubic cell. The relaxed cell volume after geometry optimisation was 3.880995 Å. The change in unit cell stress was less than 0.015 GPa in the final optimisation cycle. A custom written script was used to plot the phonon dispersion curves with grey-scale weightings reflecting the magnitude of the projected atomic displacements according to the Eigen vectors as calculated by DFPT.

Results

Thermal properties

Thermal conductivity: Combined low- and high-temperature $\kappa(T)$ data for a selection of $\text{Sr}_{1-x}\text{La}_{0.67x}\text{Ti}_{0.33x}\text{Ti}_{1-y}\text{Nb}_y\text{O}_{3-\delta}$ samples with 0% ($x = 0$), 13% ($x = 0.4$) and 27% ($x = 0.8$) vacancies are shown in Figure 1. The $\kappa(T)$ measurements confirm the suppression of the 25 K peak in $\kappa(T)$ and the emergence of phonon-glass state for the samples with 27% vacancies. Only marginal differences are evident between the 27% A-site vacancy samples sintered in air (labelled with O_3) and under 5% H_2 in N_2 (labelled with $\text{O}_{3-\delta}$), suggesting that any oxygen vacancies have a minimal

impact on $\kappa(T)$, and that the A-site vacancies are the key driver for the phonon-glass state. In all cases, the electronic contribution to κ is negligibly small due to the relatively high $\rho(T)$ of these samples (see below).

Phonon Eigen Vector Analysis: Symmetry analysis was used to obtain information on which atomic displacements contribute to the various phonon Eigen vectors at the high symmetry points in the Brillouin zone (BZ). These modes are visualised in Figure 2 and an overview of the atoms that are allowed by symmetry to enter into the various characters of the Eigen vectors at the high-symmetry points are given in Table 1. This analysis reveals that the modes that correspond to Eigen vectors of character R_4^- , M_3^- , M_5^- , X_3^- and X_5^- contain Sr displacements and can therefore be expected to be strongly affected by the vacancy engineering. Furthermore, as the characters of the phonon Eigen vectors are expected to vary continuously, lines of dispersion connecting these points, (e.g. X_5^- to R_4^- and Γ to X_3^-) will also have Eigenvectors that are dominated by A-site displacements even though by symmetry, the character of the different atoms are now allowed to mix (see Table 2). To validate this assertion, the symmetry analysis results are compared to our atom resolved calculations of the phonon dispersion, which are shown in Figure 2. This reveals that most of the phonon density of states below 130 cm^{-1} can be attributed to a single band of low-energy modes that are essentially of Sr nature with only minor Ti and O admixture. While at the zone boundaries the group velocity of the phonon modes will clearly be zero, the fact that they have significant dispersion across the BZ, means that they are expected to have a substantial effect on the low-temperature thermal transport properties. Indeed, the calculated 300 K cumulative κ_{lat} from Ref. 37, replotted in Figure 2, alongside our atom resolved phonon dispersion curves, reveals that up to 50% of the lattice conductivity is attributable to phonon modes of energy $<130 \text{ cm}^{-1}$, and that this is dominated by phonons with predominantly Sr character. As noted before,³⁷ some of the optic modes have considerable dispersion and therefore contribute to the thermal transport. Many of these heat conducting modes are dominated by Ti motions, and are mainly at higher energies. Oxygen contributes to most of the modes throughout the BZ (in keeping with the symmetry analysis in

Tables 1, 2). It should be noted that the imaginary frequencies at the R-point are due to an instability related to an octahedral rotation present as a structural distortion (Pm-3m to I4/mcm) below 110 K. The main result is hence a very striking low-energy mode that is dominated by Sr motions, which can be expected to be strongly affected and localised by the disruption of the Sr-O bonding network.

Heat capacity: C_p data (2-873 K) for SrTiO₃ and Sr_{0.8}La_{0.53}□_{0.27}TiO₃ (sintered in air) are shown in Figure 3. These data were fitted using a small electronic contribution (γT) and a combination of two Debye (θ_{Di}) and two Einstein (θ_{Ei}) modes with the total number of oscillators equal to the number of atoms per formula unit (i.e. $\sum n_i = 5$ for $x = 0$ and $\sum n_i = 4.73$ for $x = 0.8$):³⁸

$$C_p = \gamma T + \sum_{i=1}^2 \left[9n_{Di} R \left(\frac{T}{\theta_{Di}} \right)^3 \int_0^{\theta_{Di}/T} \frac{x^4 e^x}{(e^x - 1)^2} dx \right] + \sum_{i=1}^2 \left[3n_{Ei} R \left(\frac{\theta_{Ei}}{T} \right)^2 \frac{e^{\theta_{Ei}/T}}{(e^{\theta_{Ei}/T} - 1)^2} \right] \quad (1)$$

The energies and weighting of these modes are summarized in Table 3 and the quality of the fits is evident from the $C_p(T)$, $C_p/T^3(T)$ and $C_p/T(T^2)$ plots in Figure 3. The lowest energy Einstein mode ($\theta_{E2} = 17$ -19 K) accounts for the peak at ~ 4 K (Figures 3c, d). This mode has a low weighting ($n_{E2} < 0.001$) and won't be discussed any further. The weighting of the high-energy Debye mode ($n_{D1} \sim 3.1$) does not change significantly between the two samples, while it softens from 676(3) K to 617(5) K, in agreement with the presence of vacancies and increased flexibility of the structure. For SrTiO₃: $\theta_{D2} = 249(1)$ K ($n_{D2} = 1.8$) and $\theta_{E1} = 166(1)$ K with a low $n_{E1} = 0.1$. These values change to $\theta_{D2} = 223(1)$ K with a reduced $n_{D2} = 1.1$ and $\theta_{E1} = 175(1)$ K with a five-fold increased $n_{E1} = 0.5$, signalling a transfer of spectral weight from Debye into more localised Einstein modes for the phonon-glass sample. The weighted average of the Debye and Einstein temperatures (using $\theta_E/\theta_D \approx \sqrt[3]{\pi/6}$) decreases from 514(2) to 488(2) K, consistent with a softening of the lattice. The low-temperature $C_p/T(T^2)$ data are shown in Figures 3e, f and evidence significant non-linearity due to the low-energy θ_{E2} modes. The fitted values for the Sommerfeld coefficient are $\gamma = 0.2$ mJ mol⁻¹ K⁻² for SrTiO₃ and $\gamma = 0.5$ mJ mol⁻¹ K⁻² for Sr_{0.8}La_{0.53}□_{0.27}TiO₃. This suggests a non-zero density of states at the Fermi Level, $N(E_F) \neq 0$, despite these samples being electrically insulating when probed

by DC methods. However, as discussed below, impedance measurements indicate the presence of a conducting core - insulating shell microstructure, consistent with $\gamma \neq 0$.

Atomic displacement parameters: Variable temperature NPD data (4-1000 K) were collected from a $\text{Sr}_{0.20}\text{La}_{0.53}\square_{0.27}\text{TiO}_3$ sample sintered in air. A representative Rietveld fit to the 300 K dataset is shown in Figure 4a. The sample undergoes a structural phase transition from the simple cubic Pm-3m perovskite to a tetragonal I4/mcm superstructure between 473-573 K (Figure S3). The I4/mcm structure is characterised by $a^0a^0c^-$ octahedral tilting³⁹ with no evidence for the ordering of the A-site vacancies in vacancy-rich and poor layers.⁴⁰⁻⁴¹ The A-site occupancy was found to be $\text{Sr}_{0.2}\text{La}_{0.542(5)}$, confirming the presence of a near nominal amount of vacancies. The temperature dependence of the isotropic thermal displacement parameters (U_{iso}) for the Sr/La, Ti and O sites is given in Figure 4b. This plot shows that all atomic sites have significant residual disorder at 4 K, indicating that the A-site vacancies affect both the Ti and O sublattices. To facilitate fits to the $U_{\text{iso}}(T)$, a weighted average of the O U_{iso} 's on the 4c and 8d sites of the I4/mcm structure was calculated. Fits were undertaken using both the Debye and Einstein models:⁴²⁻⁴³

$$U_{\text{iso}} = \frac{3\hbar^2}{mk_B\theta_D} \left[\frac{1}{4} + \left(\frac{T}{\theta_D} \right)^2 \int_0^{\theta_D/T} \frac{x}{e^x - 1} dx \right] + d^2 \quad (2)$$

$$U_{\text{iso}} = \frac{\hbar^2}{2mk_B\theta_E} \coth \frac{\theta_E}{2T} + d^2 \quad (3)$$

The best fit to the A-site U_{iso} 's was obtained using the Einstein model, which had a ~10% lower residual, whereas the Debye model yielded slightly better fit statistics for the Ti and O sites but with little visual difference in fit quality. The presence of a significant Einstein contribution to at least one of the U_{iso} 's is consistent with the heat capacity fits. The final fitted values are: $\theta_E = 150(5)$ K (Sr/La) [$\theta_D = 260(10)$ K (Sr/La)], $\theta_D = 488(11)$ K (Ti) and $\theta_D = 664(11)$ K (O). The $\theta_E = 150(5)$ K for Sr/La is in good agreement with $\theta_{E1} = 175(1)$ K from C_p fitting, suggesting that the A-site vibrations do indeed start to become more localised. A fit to the average U_{iso} yielded $\theta_D = 454(9)$ K, in good agreement with the weighted average from the $C_p(T)$ fits ($\theta_{D, \text{av}} = 488(2)$ K). The residual disorder (d^2) values did not vary between the Debye and Einstein fits and are $d^2 = 0.0060(2)$ Å²

(Sr/La), $d^2 = 0.0095(2) \text{ \AA}^2$ (Ti) and $d^2 = 0.0124(2) \text{ \AA}^2$ (O). As can be seen from the inset to Figure 4b, the d^2 values have a linear dependence on the distance to the A-site, confirming that the atoms nearest to the A-site vacancies (O) are affected most strongly by structural disorder.

Electrical properties

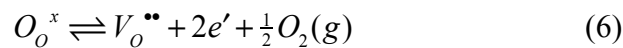
This section is split into two parts: the first deals with impedance spectroscopy measurements on electrically insulating $\text{Sr}_{0.2}\text{La}_{0.53}\square_{0.27}\text{TiO}_3$ samples sintered in air and under flowing oxygen. The second part is focussed on the electrical properties of highly conducting $\text{Sr}_{0.20}\text{La}_{0.53}\square_{0.27}\text{Ti}_{1-y}\text{Nb}_y\text{O}_{3-\delta}$ samples sintered under 5% H_2 . Both sets of results point towards an inhomogeneous core-shell microstructure.

Insulating samples: Immittance spectroscopy (IS) data for $\text{Sr}_{0.2}\text{La}_{0.53}\square_{0.27}\text{TiO}_3$ sintered in air is shown in Figure 5 and indicated the sample to be highly insulating with $\rho \gg 10^7 \text{ \Omega cm}$ at 300 K. Despite the noise due to the high sample impedance, a single semi-circular arc was observed in the complex modulus (M^*) plane plot, with a corresponding Debye-like peak in the imaginary modulus (M'') spectroscopic plot, Figure 5a. Analysis using a parallel RC element shows that this response has a capacitance, $C \sim 10 \text{ pF}$ and $\rho \sim 0.21 \text{ M}\Omega \text{ cm}$ at 300 K. The magnitude of C is typical of a bulk response for a non-ferroelectric material,⁴⁴ *i.e.* it represents a significant volume fraction of the sample. The size of the semi-circular arc and the M'' peak height remained invariant upon heating, indicating that the capacitance is relatively temperature independent. However, the M'' peak was displaced to higher frequency, indicating a decrease in time constant due to a decrease in ρ , Figure 5a. As the semi-circular arc was increasing hard to fully resolve, C and ρ were estimated from the M'' peak at each temperature according to:

$$C = \frac{\epsilon_0}{2M''_{max}} \quad (4)$$

$$\rho = \frac{1}{2\pi f_{max}C} \quad (5)$$

where ϵ_0 is the vacuum permittivity, M''_{\max} is the imaginary modulus peak height and f_{\max} is the frequency (in Hz) at which the peak maximum occurs.⁴⁵ Using this methodology conductivity values for the bulk response, b1 ($\sigma_{b1} = 1/\rho_{b1}$) were determined at each temperature at which a peak maximum was observed. The values exhibit the expected Arrhenius behaviour with an activation energy, $E_A \sim 0.33$ eV, see Figure 6. On further heating to above 700 K a further semi-circular arc appears in both the complex impedance (Z^* , Figure 5c) and modulus (M^*) plane plots with corresponding Debye-like peaks in the Z'' and M'' spectroscopic plots, Figure 5b. The peaks are spectroscopically coincident, Figure 5b, and have an associated $C \sim 3$ pF at all temperatures analysed, indicating that this is associated with a bulk-like (high volume fraction) region of the sample – assigned as b2 hereafter. With increasing temperature two lower frequency responses are increasingly evident in the impedance data, Figures 5c, d; these responses have associated C of the order 10^{-10} and 10^{-8} F and are assigned to grain boundary and electrode responses, respectively. These responses contribute very little to the total sample resistivity, ρ_T , and to a first approximation $\rho_T \approx \rho_{b2}$ (and hence $\sigma_T \approx \sigma_{b2}$). ρ_{b2} and C_{b2} values were extracted from Z^* plane plots based on a simple parallel RC model and σ_{b2} plotted as function of temperature in Arrhenius format, Figure 6. The data indicate a thermally-activated conductivity with $E_A \sim 1.40$ eV. Overall the data indicate an electrical microstructure with coexistence of two high volume fraction regions within the sample and which have significantly different conductivity. Such a microstructure, often referred to as “coring”, is well known to occur in titanate dielectrics,⁴⁶ whereby oxygen is lost during high temperature sintering releasing (conduction) electrons:



On cooling, and post densification, slow diffusion kinetics mean that these oxygen vacancies are not filled homogeneously and can result in either a semiconducting pellet interior with an insulating “skin”, or semiconducting grain interiors with an oxidised (insulating) grain shell.⁴⁵ In the case of the former, polishing can remove this layer. In our case, polishing of the sample had no effect on

the IS data indicating the latter microstructure, see Figure 6 inset. Such coring effects are not detectable by conventional DC conductivity measurements but are often visually evident by a dark grey-blue colouring below a lighter yellow-beige surface; the effect can also be exacerbated by pressing defects.⁴⁶ By contrast IS data for $\text{Sr}_{0.2}\text{La}_{0.53}\square_{0.27}\text{TiO}_3$ sintered in O_2 at 1400 °C indicates an electrically homogenous microstructure with no evidence of a conductive core. The impedance and modulus data obtained above 700 K are dominated by a single response, with associated capacitance of *ca.* 8-9 pF, characteristic of a bulk response (Figure S4).⁴⁴ As with the air-sintered sample, grain boundary and electrode effects make a small contribution to the total sample resistance but over the temperature range studied $\sigma_T \approx \sigma_b$. The bulk conductivity (σ_b) exhibits Arrhenius behaviour with $E_A \sim 1.41$ eV – very similar in both magnitude and temperature dependence to the resistive (shell) response in the air-sintered sample, Figure 6. $\text{Sr}_{0.2}\text{La}_{0.53}\square_{0.27}\text{TiO}_3$ and $\text{Sr}_{0.2}\text{La}_{0.53}\square_{0.27}\text{Ti}_{1-y}\text{Nb}_y\text{O}_{3-\delta}$ sintered in 5% H_2 in N_2 were too conductive to allow deconvolution of their electrical microstructure using immittance spectroscopy.

Conducting samples: $S(T)$, $\rho(T)$, the power factor S^2/ρ and ZT for several

$\text{Sr}_{0.20}\text{La}_{0.53}\square_{0.27}\text{Ti}_{1-y}\text{Nb}_y\text{O}_{3-\delta}$ samples ($0 \leq y \leq 0.15$) sintered under 5% H_2 are shown in Figure 7.

Small amounts of Nb substitution are known to improve S^2/ρ . The largest $S^2/\rho = 0.55$ mW m⁻¹ K⁻² (from 600-1000 K) was observed for the $y = 0.05$ sample. This is 2-3 times smaller than the best reported values for polycrystalline SrTiO_3 based thermoelectrics, thus limiting ZT to ~ 0.15 at 873 K, despite the reduction of $\kappa(T)$ and emergence of a phonon-glass state by the introduction of A-site vacancies. We note that S^2/ρ increases monotonously and does not show a peak at ~ 500 K, which is caused by the semiconducting $\rho(T)$ near room temperature. A second important observation is the non-monotonous relation between electrical conductivity, $\sigma = 1/\rho$, and S . Within a single band approximation, increases in S are linked to a reduction in carrier concentration, n , thus leading to a reduction in $\sigma = ne\mu$, where e is the electron charge and μ is the carrier mobility. For the current materials, there is no systematic $S(\sigma)$ dependence and an almost random variation is observed

(Table 4). This non-systematic variation, can be explained using a core-shell model, analogous to the samples sintered in air. Here, the shell occurs due to an increase in partial oxygen pressure upon cooling from sintering conditions under 5% H₂, leading to oxidation of the outer layer of the grains.⁴⁷ In a two-component model electrically connected in series, S and ρ are given by:⁴⁸

$$S = \frac{(1-x_s)\frac{S_c}{\kappa_c} + x_s\frac{S_s}{\kappa_s}}{\frac{(1-x_s)}{\kappa_c} + \frac{x_s}{\kappa_s}} \quad (7)$$

$$\rho = (1 - x_s)\rho_c + x_s\rho_s \quad (8)$$

Here, x_s is the volume fraction of the “insulating” shell and S_s (S_c) and κ_s (κ_c) are the S and κ of the shell (core). κ does not change much upon reduction in 5% H₂ (see Figure 1) and $\kappa \sim 2.5 \text{ W m}^{-1} \text{ K}^{-1}$ was assumed for both the core and shell regions. The measured S and ρ are therefore volume weighted averages of the core and shell regions. In order to evaluate the thermoelectric properties of the Sr_{0.20}La_{0.53}□_{0.27}Ti_{1-y}Nb_yO_{3-δ} samples reported here, we use the near universal S(ρ) relationship for La and Nb substituted SrTiO₃ crystals.⁴⁹⁻⁵⁰ The variation in S spans 1-2 orders of magnitude (10s-1000s μV K⁻¹), while ρ varies by 4-5 orders of magnitude. The impact of the shell is therefore much more pronounced on ρ than it is on S. Previous work making an explicit comparison between single and polycrystalline Sr_{1-x}La_xTiO₃ (x < 0.05) suggested a ~ 70 nm thick insulating acceptor layer.⁵¹ Assuming a similar 50 nm insulating shell and cube shaped grains with 10 × 10 × 10 μm³ dimensions, this leads to a 0.3 volume % fraction of shell material. Using the measured S, and the S(ρ) relation this enables an estimate of ρ_c and of ρ_s, as summarized in Table 4. For the Sr_{0.20}La_{0.53}□_{0.27}Ti_{1-y}Nb_yO_{3-δ} samples, the values of ρ_s fall within a factor of five, between 8-40 Ω cm. This shows that the shell region remains reasonably conducting but is resistive enough to lead to an 1-2 order of magnitude increase in ρ at 300 K, thereby severely reducing the maximum attainable S²/ρ. At higher temperatures, the impact of the insulating shell is reduced and ρ(T) takes its usual metal-like form and S²/ρ is 50-60% reduced compared to samples without vacancies.

The semiconducting $\rho(T)$ near room temperature can be used to obtain an estimate of the activation energy, E_A for carrier transport through the shell. Inspection of a $\log\rho(1/T)$ plot for the $\text{Sr}_{0.20}\text{La}_{0.53}\square_{0.27}\text{Ti}_{1-y}\text{Nb}_y\text{O}_{3-\delta}$ samples reveals linear, thermally activated, behaviour between 300-580 K for the most insulating ($y = 0$, $y = 0.15$) samples, and 300-380 K for the more conducting $y = 0.05$ and $y = 0.1$ samples (Figure S5). The $y = 0$ sample was found to have $E_A = 0.147(3)$ eV, while the Nb substituted samples have similar $E_A = 0.098(3)$ eV (Table S1). We note that these values are much lower than observed from immittance spectroscopy on samples sintered in air ($E_A \sim 1.4$ eV), where the shell is truly insulating. This analysis also suggests that the presence of Nb to some degree prevents the formation of the insulating shell upon cooling the samples.

Discussion

Thermal transport: Low-temperature $\kappa(T)$ data confirms the presence of a vacancy induced phonon-glass state, while C_p fitting demonstrates a transfer of spectral weight into a $\omega_E \sim 120$ cm^{-1} Einstein mode, which is centred on a line of dispersion observed in the first principles phonon calculations and whose character is dominated by Sr displacements. Symmetry analysis was used to visualise the low-energy modes at the high-symmetry points and these are indeed dominated by Sr motions (Figure 2). The change in C_p signals a significant localisation of the heat carrying phonon modes upon the introduction of A-site vacancies, consistent with the removal of a large fraction (27%) of the Sr-O chemical bonds, leading to a flattening of the Sr dominated phonon modes. The experimental data therefore suggests that breaking of chemical bonds underpins the observed phonon-glass state, and that it is not only attributable to mass disorder in an otherwise “rigid” phonon band structure. The residual disorder that is apparent from the thermal displacement parameters affects all atomic sites, with the largest d^2 for the nearest neighbour to the vacancy (O), followed by Ti and then Sr/La. This is in keeping with recent high-resolution STEM imaging, which reveals that all sites are affected by the introduction of A-site vacancies.²⁸ The interpretation of this residual disorder is in terms of static displacements from the equilibrium position that is

enabled by the removal of many of the Sr atoms. This disorder will impact on $\kappa(T)$ but the magnitude of the displacements ($d < 0.11 \text{ \AA}$ for O at 2 K) remains small, in particular compared to thermal motion at elevated temperatures, where the glass state survives, so cannot be the dominant contribution to reduction of $\kappa(T)$.

Electrical: Both impedance and DC electrical measurements reveal the presence of core-shell grain structures, which increase ρ and limit S^2/ρ . Removal of these oxidised shell regions will significantly enhance the thermoelectric performance, particularly at medium temperatures (450-500 K), where S^2/ρ usually peaks. At high-temperatures ($> 600\text{-}700 \text{ K}$), $\rho(T)$ returns to the metal-like dependence that is expected for degenerately doped SrTiO_3 , and the impact of the insulating shell is much reduced with a 50-60% reduction compared to SrTiO_3 samples without A-site vacancies. A-site vacancies open-up the perovskite structure and increase oxide ion conductivity.⁵² It is therefore perhaps unsurprising that the formation of an insulating shell is exacerbated in samples with higher concentrations of A-site vacancies. Indeed, 5% H_2 reduced samples with no and 7% vacancies do not show the near room temperature semiconducting tail, while samples with 13% and 27% vacancies do.²² Removal of the oxidised shells will enable strongly improved S^2/ρ near 500 K, while the gain at high-temperatures is expected to be smaller. It will thus help with creating a larger temperature-averaged power factor and broader high-ZT plateau, both of which are key features in improving power output and efficiency of a thermoelectric device. This work demonstrates that during cooling from sintering conditions in a 5% H_2 in N_2 atmosphere, the oxygen partial pressure increases sufficiently for an oxidized shell to form at intermediate temperatures, after which the sample is kinetically trapped in a non-equilibrium core-shell state. Formation of this layer could be prevented by buffering the $p\text{O}_2$ upon cooling or rapid quenching of the samples.

Conclusions

In conclusion, we have investigated the vacancy induced phonon-glass state in A-site deficient $\text{Sr}_{1-x}\text{La}_{0.67x}\square_{0.33x}\text{TiO}_3$ and the electrical transport in reduced $\text{Sr}_{0.20}\text{La}_{0.53}\square_{0.27}\text{Ti}_{1-y}\text{Nb}_y\text{O}_{3-\delta}$ samples. The phonon-glass state not only results from the large mass disorder created on the perovskite A-site, but can be linked directly to the removal of the Sr-O bonds, leading to localisation of specific low-energy heat carrying Sr-O phonon modes. The electrical properties are dominated by a heterogeneous core-shell grain microstructure, which limits the electrical conductivity and thus the power factor. If the grain boundary structure can be controlled, whilst maintaining the A-site defect chemistry, significant improvements in power factor and device figure of merit are possible.

Acknowledgements

SRP and JWGB acknowledge the EPSRC (grant EP/N01717X/1) and Leverhulme Trust (grant RPG-2012-576) for financial support and the STFC for provision of beam time at ISIS. FDM acknowledges the EPSRC for financial support (grant EP/P024637/1). MSS acknowledges the Royal Society for a University Research Fellowship (grant UF160265). Raw data underpinning this work is available from the Heriot-Watt data repository.

Supplementary Information

Crystallographic information from Rietveld analysis of laboratory X-ray and neutron powder diffraction; laboratory X-ray powder diffraction patterns; Scanning Electron Microscopy data; additional immittance spectroscopy data and Arrhenius fits to the near room temperature DC electrical resistivity data.

Table 1. Symmetry-allowed atomic displacements (phonon character) at high-symmetry points of the Brillouin Zone (BZ) for a $Pm-3m$ ABO_3 perovskite structure. The “X” indicates that displacements of that atom type are allowed by symmetry for that irreducible representation (IR). Note that the segregation between A and B site displacements is almost complete at the high-symmetry BZ points, indicating that A and B site motions are not coupled. Labels for the IRs are as tabulated in the web-based program ISODISTORT based on the $Pm-3m$ perovskite structure with A $1a$ (0,0,0), B $1b$ ($\frac{1}{2}$, $\frac{1}{2}$, $\frac{1}{2}$), O $3c$ (0, $\frac{1}{2}$, $\frac{1}{2}$).

Irreducible Representations		A	B	O
[0 0 0]	Γ_4^-	X	X	X
	Γ_5^-	-	-	X
$[\frac{1}{2} \frac{1}{2} \frac{1}{2}]$	R_5^+	-	X	-
	R_2^-	-	-	X
	R_3^-	-	-	X
	R_4^-	X	-	X
	R_5^-	-	-	X
$[\frac{1}{2} \frac{1}{2} 0]$	M_1^+	-	-	X
	M_2^+	-	-	X
	M_3^+	-	-	X
	M_4^+	-	-	X
	M_5^+	-	-	X
	M_2^-		X	X
	M_3^-	X	-	-
	M_5^-	X	X	X
$[\frac{1}{2} 0 0]$	X_1^+	-	X	X
	X_2^+	-	-	X
	X_5^+	-	X	X
	X_3^-	X	-	X
	X_5^-	X	-	X

Table 2. Symmetry-allowed atomic displacements (phonon character) at lower symmetry lines of the Brillouin Zone (BZ) for a $Pm-3m$ ABO_3 perovskite structure. The “X” indicates that displacements of that atom type are allowed by symmetry for that irreducible representation (IR). Note that motions of both A and B are now often symmetry allowed within an IR, leading to coupling between A, B and O site motions. Labels for the IRs are as tabulated in the web-based program ISODISTORT based on the $Pm-3m$ perovskite structure with A $1a$ (0,0,0), B $1b$ ($\frac{1}{2}$, $\frac{1}{2}$, $\frac{1}{2}$), O $3c$ (0, $\frac{1}{2}$, $\frac{1}{2}$).

Irreducible Representations		A	B	O
[$\frac{1}{2}$ $\frac{1}{2}$ γ]	T1	X	-	X
	T2	-	-	X
	T3	-	X	X
	T4	-	-	X
	T5	X	X	X
[α $\frac{1}{2}$ α]	S1	X	X	X
	S2	X	-	X
	S3	X	X	X
	S4	-	X	X
[α α α]	LD1	X	X	X
	LD2	-	-	X
	LD3	X	X	X
[α α 0]	SM1	X	X	X
	SM2	X	X	X
	SM3	X	X	X
	SM4	-	-	X
[α 0 0]	DT1	X	X	X
	DT2	-	-	X
	DT5	X	X	X
[α $\frac{1}{2}$ 0]	Z1	X	X	X
	Z2	-	X	X
	Z3	X	X	-
	Z4	X	X	-